Pergamon

Journal of Structural Geology, Vol. 20, No. 2/3, pp. 255 to 267, 1998

0191-8141/98 $19.00 + 0.00

PII: S0191-8141(97)00058-8

Texture of Solnhofen limestone deformed to high strains in torsion

MARTIN CASEY,* KARSTEN KUNZE and DAVID L. OLGAARD†

Geologisches Institut, ETH-Z, CH-8092, Zürich, Switzerland

(*Received* 7 *January* 1997; *accepted in revised form* 5 *August* 1997)

Abstract—Solnhofen limestone was deformed in torsion to shear strains (γ) ranging from 1 to 12, at a temperature of 750°C, 300 MPa confining pressure and a maximum strain-rate of $10^{-3}\,s^{-1}$. These deformation conditions correspond to the intracrystalline power-law dislocation creep field close to the boundary to the grain-size-sensitive superplastic creep field.

The grain-shape microstructure was observed using orientation contrast by backscattered electrons in the SEM. The grains remain sub-equant with an average grain size of around 4 μm, even to the highest strains.

Lattice preferred orientation was determined using both X-ray texture goniometry and automated electron backscatter diffraction. The *c*-axis preferred orientation develops from two main maxima with a weak sub-maximum, through two maxima to a single maximum perpendicular to the shear plane. The rate of increase of the intensity of the single maximum with increasing strain diminishes, and it appears that there is a tendency to a steady-state texture. The final single *c*-axis maximum is displaced slightly towards the shortening direction of the applied simple shear. The *a*-axes tend to a girdle perpendicular to the *c*-axis maximum.

It is proposed that the partitioning of deformation between intra- and inter-crystalline mechanisms results in a pulsating strain state in the grains, contributing to the maintenance of sub-equant grains. It is argued that the lattices of constituent grains rotate continuously with no stable end orientation and that this can lead to a steady-state texture.

The experimental preferred orientation compares well with that of natural calcite mylonites in the position of the *c*-axis maximum and the *a*-axis girdle. © 1998 Elsevier Science Ltd.

INTRODUCTION

Natural deformation of rocks to high strains produces characteristic microstructures of the grains and characteristic crystallographic preferred orientation (Riekels and Baker, 1977; Schmid *et al.*, 1981; Dietrich and Song, 1984). The motivation has been to make a link between the observations and the conditions of the deformation such as kinematics, strain-rates, temperature, stress levels and operative slip-systems. The processes involved in the crystallographic preferred orientation development during deformation have been the topic of much observation (Law *et al.*, 1986; Schmid and Casey, 1986; Law, 1987). Many models for the development of preferred orientation have been put forward (Lister *et al.*, 1978; Lister and Paterson, 1979; Lister and Hobbs, 1980; Wenk *et al.*, 1989). The observational studies have usually made empirical comparisons between the observed microstructure and crystallographic preferred orientation and the known or surmised conditions of deformation. This approach has been criticized by Wenk and Christie (1991), because the conclusions are not based on well-founded physical concepts such as the Taylor–Bishop–Hill method. Although the view of Wenk and Christie (1991) that interpretations should be based on rigorous physics is perfectly correct, the precise micromechanical basis for models of preferred orientation development is not certain. Much insight into the problem can be expected from laboratory experiments on natural rock materials under simple shear kinematics and deformation conditions chosen so as to give the same deformation mechanisms as in natural deformations. Until now, the experimental difficulties have restricted the number of studies for simple shear kinematics to those of Friedman and Higgs (1981), Kern and Wenk (1983) and Schmid *et al.* (1987) for calcite, and Dell'Angelo and Tullis (1989) for quartz. Such work has been much needed to provide tests for the conclusions of the empirical approach and to indicate better which physical principles should be used for the more rigorous model studies.

The recent development of the torsion technique by Paterson now allows routine torsion testing at high temperatures and pressures to almost any chosen value of shear strain to greater than 10. The parallel development of the electron backscatter diffraction (ebsd) method of measuring local crystallographic preferred orientation has enabled results to be obtained from the small specimens produced by the torsion method.

SOLNHOFEN LIMESTONE AND ITS DEFORMATION MECHANISMS

Solnhofen limestone has been extensively studied in the laboratory. Its rheology has been well established in uniaxial compression experiments by Rutter (1974), Schmid (1976), Schmid *et al.* (1977) and Walker *et al.* (1990). These studies identify three deformation regimes

*Present address: Department of Earth Sciences, The University, Leeds LS2 9JT, U.K.

†Present address: Exxon Production Research, P.O. Box 2189, Houston, TX 77252, U.S.A.

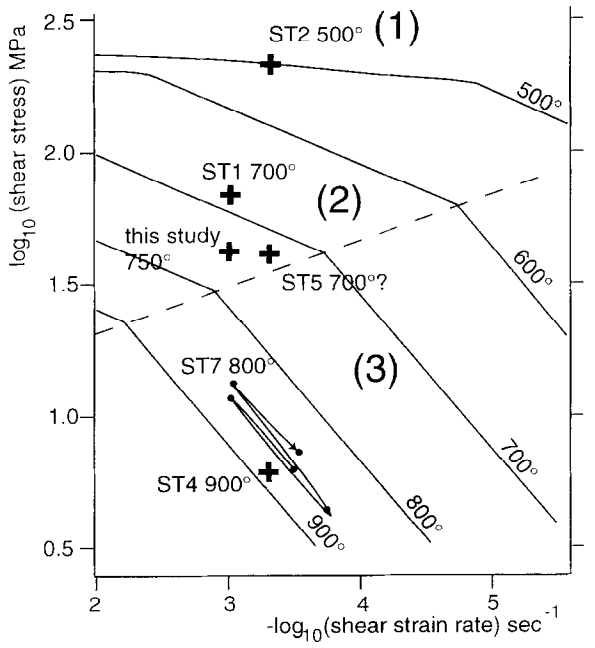

Fig. 1. Flow regimes of Solnhofen limestone plotted on a log stress vs log strain-rate graph (after Schmid *et al.* (1977)).

on the basis of flow law and microstructure (Fig. 1). The regimes consist of a high-stress regime with an exponential flow law ($\dot{\gamma} \propto \exp(\tau)$; regime 1), an intermediate stress regime with a power law ($\dot{\gamma} \propto \tau^n$ with $n = 4.7$; regime 2) and a low-stress, grain-size-sensitive regime also with a power law, but in this case $n = 1.7$ (regime 3). The dominant mechanisms are inferred to be twinning and dislocation glide for regime 1, dislocation creep for regime 2 and diffusion accommodated grain boundary sliding for regime 3.

Solnhofen limestone has impurity phases which pin the grain boundaries and inhibit grain growth (Rutter, 1984; Olgaard and Evans, 1988; Walker *et al.*, 1990). This makes this rock particularly suited for experimental conditions where the deformation mechanism is grain-size-sensitive. Previous work of Schmid *et al.* (1977, 1987) report optical microstructures for regimes 2 and 3. For regime 2, they report flattened grains, undulose extinction and the formation of sub-grains. Further, they report serrate grain boundaries and no signs of grain boundary migration for regime 2. For regime 3, they observed straight grain boundaries and equiaxial grains, concluding that the straight grain boundaries are the result of grain boundary migration. It can be concluded from the previous work on Solnhofen limestone that significant recrystallization does not occur under conditions close to the boundary of deformation regimes 2 and 3.

Parallel studies of the preferred orientation development by Wenk *et al.* (1973), Casey *et al.* (1978) and Rutter *et al.* (1994) show that the preferred orientation develops strongly in regimes 1 and 2 and very slowly in regime 3. The latter observation indicates that the mechanisms of dislocation creep and grain boundary sliding occur in parallel. Solnhofen limestone possesses an initial preferred orientation that is radially symmetric about the pole to bedding planes (Wenk *et al.*, 1973) (Fig. 5a). This initial preferred orientation can be exploited in studying the development of preferred orientation in that it allows a parallel study of the simple movement of maxima in pole figures in response to grain rotations, and of the development of new maxima by the rotation of pole normals to a particular orientation.

Schmid *et al.* (1987) deformed Solnhofen limestone in shear in all three regimes to shear strains of γ around 1.0. Their results form an excellent basis for the present study in which the material was deformed under conditions close to the regime 2–regime 3 boundary to shear strains from 1 to 12.0. A comparison of our results and their results is made below.

EXPERIMENTAL TECHNIQUE

Cylindrical specimens of Solnhofen limestone, cored perpendicular to bedding, were deformed in torsion at a temperature of 750°C and 300 MPa confining pressure in a Paterson Instruments deformation apparatus. The maximum strain-rate on the surface of the sample was $10^{-3}\,s^{-1}$. The deformation conditions and strain attained for the samples reported are shown in Table 1. The specimen designators consist of a root that is the laboratory experiment number, followed by a colon and a number. For the series of experiments reported here, the number gives the amount of shear strain. For the experiments of Schmid *et al.* (1987), the number gives the temperature of deformation in degrees Celsius. The deformation is shown schematically in Fig. 2. The top of the specimen is rotated anticlockwise relative to the fixed base. This technique allows large strains to be accomplished under constant conditions. The theory of the torsion test has been described in Handin *et al.* (1960), where it is demonstrated that the instantaneous strain at any point in the cylindrical specimen is simple shear. The shear strain and strain-rate are constant with position parallel to the axis of the specimen, but are

Table 1. Experimental conditions for the experiments of this study (sl series) and of Schmid *et al.* (1987) (ST series)

Sample	T (°C)	γ	P (MPa)	Strain rate (s^{-1})
Torsion				
sl5:1	750	1.	300	1.0×10^{-3}
sl1:3.5	750	3.5	300	1.0×10^{-3}
sl8:6.9	750	6.9	300	1.0×10^{-3}
sl2c2:9.6	750	9.6	300	0.75×10^{-3}
sl2c3:12	750	12.0	300	1.0×10^{-3}
Oblique shear				
ST2:500	500	1.22	250	5.0×10^{-4}
ST1:700	700	1.07	250	1.0×10^{-3}
ST5:700	700	0.92	200	5.1×10^{-4}
ST7:800	800	1.13	200	1.0×10^{-3}
ST4:900	900	1.36	200	5.1×10^{-4}

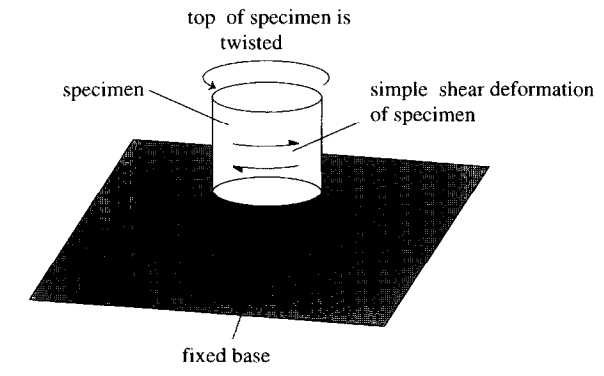

Fig. 2. Schematic illustration of the torsion experiment.

linearly proportional to the distance from the cylinder axis. The maximum strain-rate and strain therefore occur at the outer cylinder surface of the specimen. The specimens were 15 mm in diameter and 3–10 mm in length. Texture determinations and microstructural observations were carried out on surfaces that are axis-parallel, and chords to the circular sections of the specimens (Fig. 3). On these surfaces, there will be variation in the deformation caused by intersecting different radial depth of the specimen, and by a different orientation of the shear direction with respect to the surface plane normal.

The maximum shear strain in the specimen can be varied by rotating the top of the specimen through varying angles or by varying the specimen height. The specimens were enclosed in iron jackets which had scratched marker lines defining a lineation parallel to the axis of the specimen. This lineation served as a strain marker indicating the homogeneity of strain on the cylinder mantle. In all the experiments reported here, there was no detectable departure from homogeneity of strain parallel to the cylinder axis.

The measurement of preferred orientation is complicated because the shear direction, being always perpendicular to the radial direction, varies continuously around

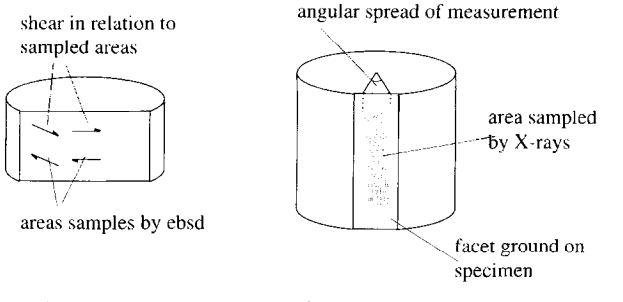

Fig. 3. Measurement areas in ebsd and X-ray texture goniometer methods. The texture is constant when referred to the radial direction. The width of the X-ray beam means that angular deviations result from the variation of the radial direction.

the cylindrical specimen. Two methods of measurement of preferred orientation were used for this study: conventional X-ray texture goniometry and individual point determinations of lattice orientation using electron back scatter diffraction (ebsd). Both these methods take observations from a flat surface ground on the cylinder (Fig. 3).

The X-ray textures were carried out with a Scintag XDS 2000 goniometer with Cu K_α radiation and a solid state detector. The energy resolution of the solid state detector enables the K_β line to be removed without a physical filter and hence gives much improved X-ray intensities. To minimize the problems caused by the variation of the shear direction the area sampled was as small as possible in the dimension perpendicular to the cylinder axis. For the X-ray goniometer, a collimator of 0.5 mm was used that gave an effective sampling width of 2 mm. X-ray pole figures were determined using the reflection mode, transmission mode technique. The reflection mode data were collected from a facet ground near the outer wall of the cylindrical specimen. The thin section for transmission mode was prepared from the surface of the reflection mode specimen, to avoid any influence of the variation of the strain state in the radial direction. Pole figures were measured for the planes 012, 104, 110, 113, 202, overlapping 024 and 018, and 116 for the undeformed material and specimens sl1:3.5, sl5:1 and sl8:6.9. The peak 006 was also measured for the undeformed material and specimens sl5:1 and sl8:6.9 (see Table 2). The relatively wide sampling area of the X-ray goniometer limited the applicability of this method to the outer part of the specimen.

Data were processed using the harmonic method of Bunge (1969), Bunge and Wenk (1977) and Casey (1981). The coordinate systems for pole figures and inverse pole figures are as defined in Casey (1981). The origin of the azimuth angle for pole figures is at N, and the origin for the co-latitude is in the centre of the pole figure. The origin for the azimuth angle of the inverse pole figures is at the first-order prism (100), and the origin of the co-latitude is parallel to the c-axis. The Euler angle convention uses angles ψ_1, ϕ and ψ_2, which are identical to the angles φ_1, ϕ and φ_2 of Bunge (1969).

Electron backscatter diffraction (ebsd) is a technique to measure the crystallographic lattice orientation at well-defined locations on the specimen surface with a spatial resolution of about 1 μm (Venables and Harland, 1973; Dingley and Baba-Kisle, 1986). Automated analysis of ebsd patterns as employed in Orientation Imaging Microscopy (Adams *et al.*, 1993) allows the determination of the orientation distribution even from small areas within heterogeneously deformed samples. It has been successfully applied to quartzite (Kunze *et al.*, 1994a) and calcite (Kunze *et al.*, 1994b) microstructures. Textures obtained by automated ebsd compare well with data from X-ray and neutron goniometry.

The observation of orientation contrast in backscatter electron images and of electron backscatter diffraction

Table 2. Diffraction peaks used for the X-ray texture determination

Number	$2\theta^\circ$ Cu K_α	Index	Letter designation	Polar angle	Azimuth	Intensity
1	23.02	012	*f*	63.1	60.0	1.0
2	29.40	104	*r*	44.6	0.0	1.0
3	31.40	006	*c*	0.0	0.0	1.0
4	35.96	110	*a*	90.0	30.0	1.0
5	39.40	113		66.3	30.0	1.0
6	43.14	202	*h*	75.8	0.0	1.0
7	47.49	024	*f*	63.1	60.0	0.15
		018	*e*	26.3	60.0	0.85
8	48.41	116		48.8	30.0	1.0

patterns in particular requires a very gentle surface preparation, because the measured signal arises from a surface layer less than 1 μm thick. After mechanical polishing, the remaining surface damage (Bilby layer) was reduced by a lapping procedure using colloidal silica suspension with a particle size of 0.025 μm. Even this technique did not prevent the opening of voids and loss of grain fragments at the surface. Surface charging has been reduced by applying an accelerating voltage of 12 kV for ebsd and 15 kV for backscattered electron imaging, and by a very thin carbon coating of about 3 nm thickness. This allowed the acquisition of indexable ebsd patterns from the same specimen imaged in orientation contrast.

The ebsd texture measurements of sl2c2:9.6 and sl2c3:12 were both taken on the same section cut, but at different locations relative to the cylinder axis, and therefore represent different amounts of finite strain. Sample sl2c2:9.6 was located in the centre of the section cut, while sample sl2c3:12 was positioned close to the left-hand outside edge (total width 10 mm, 4 mm off centre). Each of the measurement sets was taken on a patch of 1 mm square, which was sampled on a raster of 10 μm increment, resulting in a data set of more than 10,000 single orientation measurements for each area. With an average grain size of 4 μm, the chance of measuring the same grain twice is very small. About one-third of the measurements showed poor reliability of the indexing procedure as given by the confidence index (CI < 10%). This is mainly attributable to rather poor ebsd contrast for these measurements because of imperfections on the sample surface (see Fig. 4) as well as the high frequency of grain boundary hits (with a sampling patch of 1 μm diameter in a microstructure of 4-μm grain size). The sub-set of low confidence measurements does not show any preferred orientation. Therefore, possible failures in the indexing procedure for these measurements may have only a minor influence on the random background in the orientation distribution without changing the lattice preferred orientation significantly. ODFs and pole figures were calculated from the single orientation data by conventional convolution with a Gaussian distribution of 10° halfwidth. The *a* (110) pole figures and inverse pole figures were intentionally symmetrized by the inversion symmetry to produce results in a format comparable to the X-ray data.

GRAIN-SHAPE MICROSTRUCTURE

The grain-shape microstructure was observed using orientation contrast by backscattered electrons in the scanning electron microscope. The grain-shape microstructures in the undeformed material and the deformed specimen sl2c2:9.6 ($\gamma = 9.6$) are shown in Fig. 4(a & b), respectively. The grain-size of both undeformed and deformed material is around 4 μm, indicating the lack of grain growth during the experiment. The grains in the deformed state show a slight elongation in a direction about 10° to the shear direction. The orientation of the extension direction corresponding to a shear strain of $\gamma = 9.6$ is 6°. The grain boundaries of the deformed material are straight, comparable to the optical microstructures of Schmid *et al.* (1987).

TEXTURE RESULTS

The results of the present series of experiments show a progressive development of the preferred orientation with increasing applied shear strain. The results are discussed in terms of the evolution of the *c*- and *a*-axis pole figures, selected sections through the orientation distribution function (ODF) and inverse pole figures. Pole figures provide a characterization of the development of preferred orientation, which lends itself well to a correlation of field and laboratory results. The ODF allows the identification of the most preferred orientations of the crystal lattice, which in turn allows an analysis of the orientation of the slip systems relative to the imposed deformation. Inverse pole figures for the specimen directions, such as shear plane normal and shear direction, show whether particular crystal directions align preferentially parallel to the specimen directions and are potentially useful in the identification of slip systems. A comparison is made to the findings of Schmid *et al.* (1987), who performed experiments under different conditions of temperature and strain rate to shear strain around $\gamma = 1$.

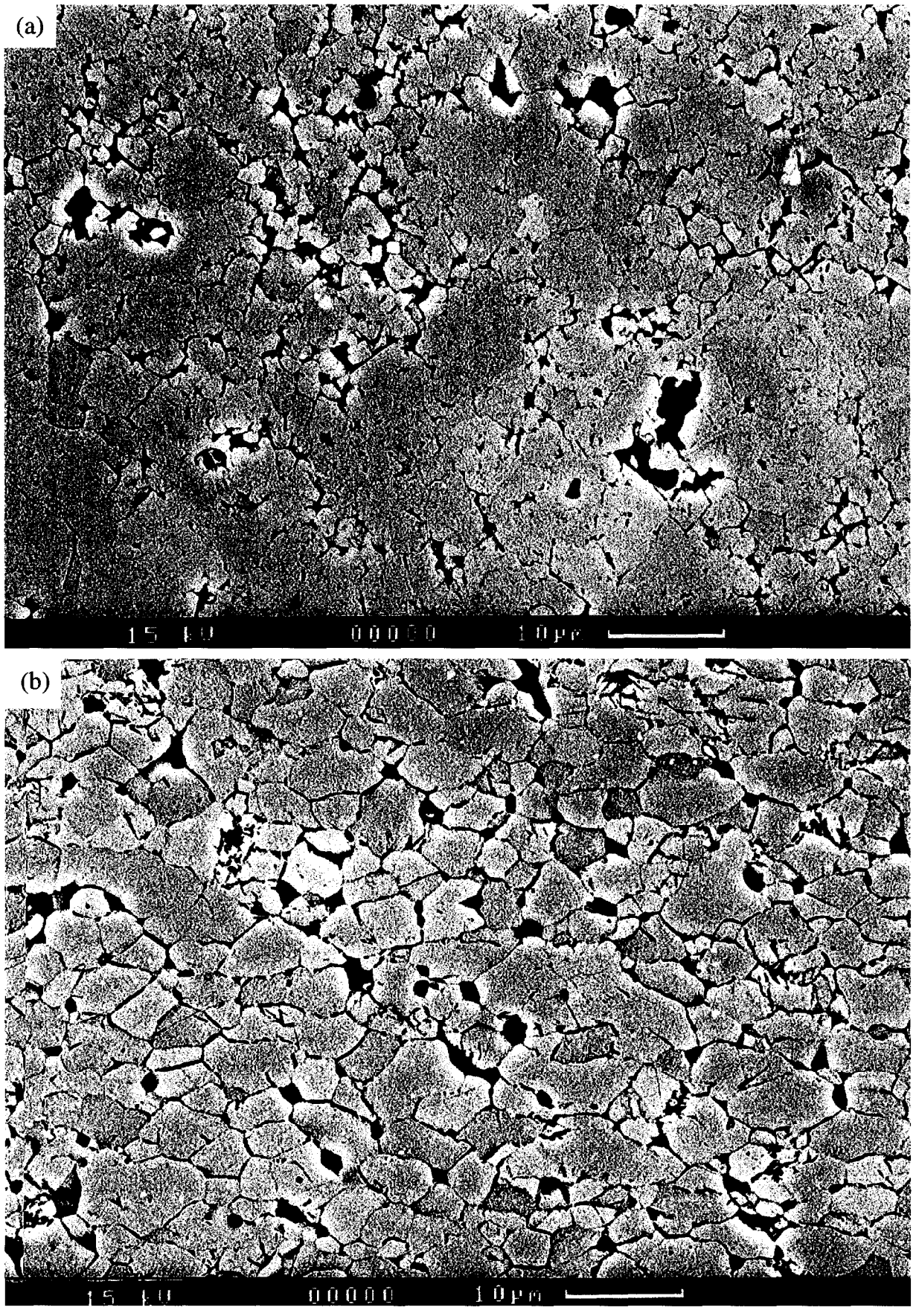

Fig. 4. Grain-shape microstructure of (a) undeformed material and (b) specimen sl2c2:9.6 in SEM backscatter electron contrast images. For specimen sl2c2:9.6, the deformation was dextral with the shear plane horizontal.

Pole figures for c- and a-axes

Pole figures for c- and a-axis directions are shown in Fig. 5. The pole figures are presented with the shear plane normal at N and the shear direction E–W. The undeformed material has the bedding plane normal at N. The results of Schmid *et al.* (1987) for the development of the c-axis preferred orientation are shown in Fig. 6. The shear values and other experimental conditions for the specimens are given in Table 1. Solnhofen limestone has a significant initial preferred orientation giving a girdle of c-axes lying in the bedding planes (Fig. 5a). The a-axis shows a point maximum perpendicular to bedding (Fig. 5g). The initial c-axis distribution for the work of Schmid *et al.* (1987) is shown in Fig. 6(f), which is the pole figure from Fig. 5(a) rotated to the appropriate orientation relative to the shear plane as described above. As will be discussed below, the development of preferred orientation in the experiments is strongly affected by simple rotations of the initial preferred orientation, and consequently, all the c-axis pole figures have indications of the amount of rotation corresponding to a rigid body rotation under the applied shear strain.

The sequential development of the c-axis pole figures is shown in Fig. 5(b–f). Three maxima are distinguished for the c-axis pole figures, labelled 1, 2 and 3, following Schmid *et al.* (1987) (Fig. 6a). Maximum 1 is at the shear plane normal, maximum 2 is on the periphery 30° anticlockwise from the shear direction, and maximum 3 is on the periphery 30° clockwise from the shear direction. For the current study, maximum 2 is only very weakly developed in the lowest strain experiment (Fig. 5b), in comparison to Schmid *et al.* (1987) (Fig. 6a). This is a consequence of the different initial c-axis distributions. The maximum 2 of Fig. 6a is mainly the result of the movement of the initial c-axis girdle.

With increasing applied shear strain, there is a progressive evolution of the c-axis pattern (Fig. 5b–f). Maximum 2 disappears. Maximum 3 weakens and rotates towards the shear plane normal, ultimately merging with maximum 1. At the highest shear strains, there is only one maximum perpendicular to the shear plane but slightly displaced towards the shortening direction of the imposed shear. Although maximum 1 continually increases in intensity with increasing shear strain, the pattern appears to be reaching a steady-state,

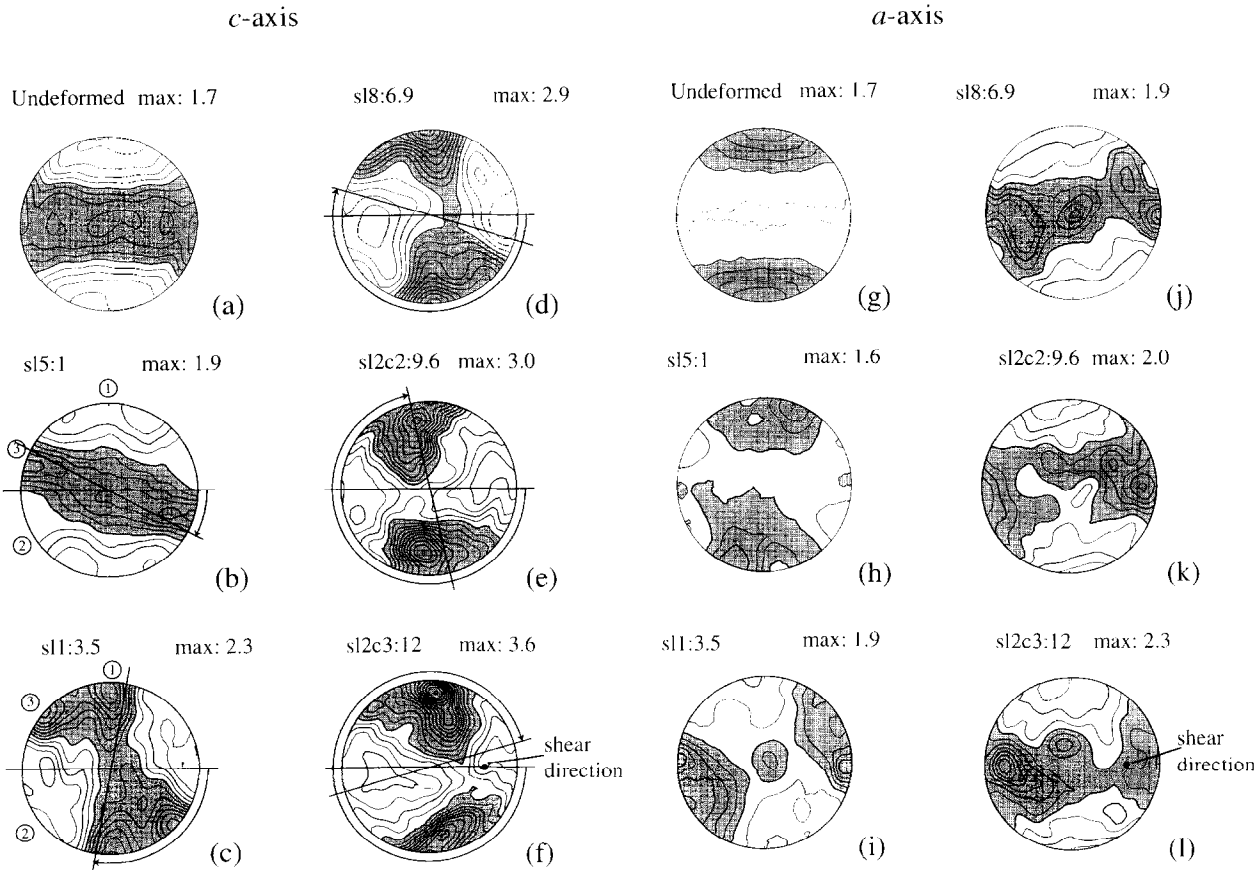

Fig. 5. (a)–(f) c-axis pole figures. (g)–(l) a-axis pole figures for specimens. The figures are upper-hemisphere equal area projection; the contour interval is 0.1 times a uniform distribution for (a) and (g) and 0.2 times a uniform distribution for the remainder. Areas above 1.0 are shaded. The shear was dextral. The solid horizontal line represents the shear plane, and the shear direction was E–W, except for sl2c3:12 where it was in the orientation shown. The oblique solid line and the arrow represent the reorientation of the ridge of the initial girdle under rigid rotation corresponding the amount of applied shear strain.

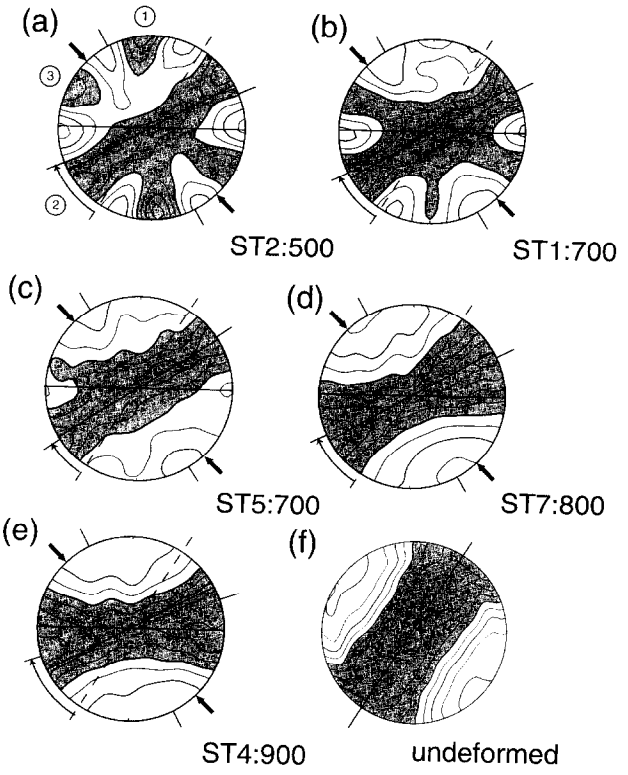

Fig. 6. (a)–(f) *c*-axis pole figures of specimens from Schmid *et al.* (1987). The figures are upper-hemisphere equal area projections. The contour interval is 0.2. Areas above 1.0 are shaded. The dashed line represents the initial girdle. The oblique solid line is the position to which the initial girdle would re-orient under a rigid rotation. The applied shear was dextral, and the horizontal solid line represents the shear plane. The bold arrows give the instantaneous shortening direction of the applied simple shear. The shear direction was E–W.

as shown by the broad similarity of the pole figures in Fig. 5(e & f).

The *a*-axis pole figures (Fig. 5g–l) show an evolution from the point maximum of the initial distribution to a girdle perpendicular to the *c*-axis point maximum (Fig. 5l). There are subsidiary maxima on the girdle.

The results of Schmid *et al.* (1987) in Fig. 6 show the effect of changing deformation conditions on the initial development of the *c*-axis preferred orientation. The *c*-axis pole figures in Fig. 6 are arranged in order of increasing temperature, beginning with ST2:500 in deformation regime 1, progressing through ST1:700 and ST5:700 in regime 2 to ST7:800 and ST4:900 in regime 3. The degree of development of the three maxima decreases from ST2:500 through ST1:700 to ST5:700, that is with increasing temperature and decreasing stress. The broad girdle running from NE to SW across the pole figures is the rotated and modified initial girdle. With increasing temperature and decreasing stress, the amount of the rotation of the girdle increases to equal the rigid rotation of the applied shear deformation, shown on the pole figures by the arcuate arrow. The results for ST7:800 and ST4:900 show predominantly a rotation of the initial *c*-axis girdle by an amount approximately equal to the rigid body rotation of the applied simple shear. There is a tendency to form subsidiary maxima near the periphery.

Allowing for the effect of the different initial preferred orientations on the development of the *c*-axis pole figure in this study, specimen sl5:1 (Fig. 5b) compares well with the corresponding experiment of Schmid *et al.* (1987), specimen ST5:700 (Fig. 6c). This supports the use of torsion experiments to study the effects of simple shear deformation.

Sections through the ODF

Sections through the ODF for the undeformed material, specimen sl5:1 and specimen sl1:3.5 are shown in Fig. 7. The sections are chosen to show the significant detail of the ODFs. The value of $\phi = 90°$ places the *c*-axis at the periphery of the pole figure. The value of ψ_1 determines the azimuth of the *c*-axis. Variation with ψ_2 corresponds to a rotation about the *c*-axis so that all points on the vertical lines in Fig. 7 represent the same *c*-axis orientation with continuously varying *a*-axis orientations. Away from the chosen sections, the values of probability are close to zero. For the undeformed material, there is nearly no preferred orientation in rotation about the *c*-axis (Fig. 7a, variation with ψ_2). The *c*-axis pole figure of the lowest strained sample (sl5:1) shows a predominant simple rotation of the initial

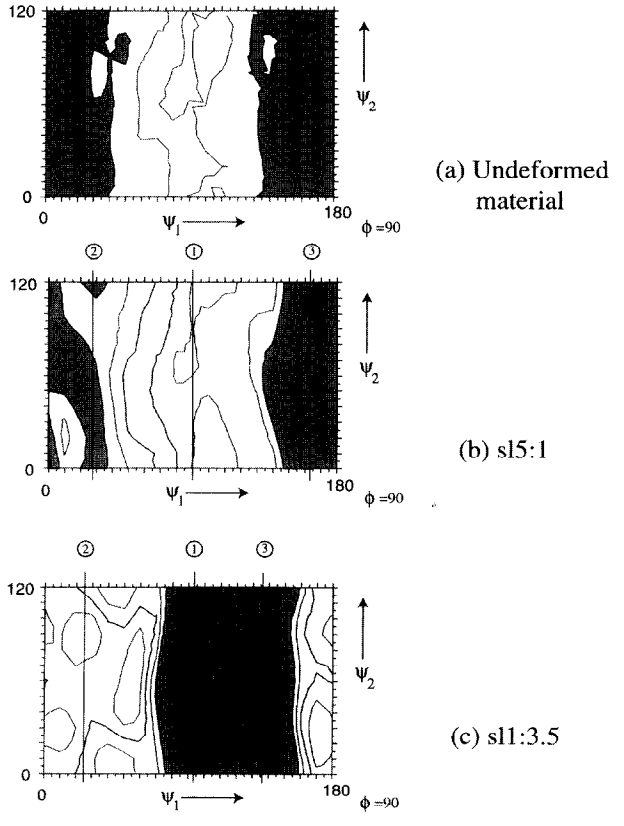

Fig. 7. Orientation distribution function sections for (a) the undeformed material, (b) specimen sl5:1 and (c) sl1:3.5. The figures are contoured in multiples of 0.25 times a uniform distribution. Areas above 1.0 are shaded. Areas above 2.25 are shaded more darkly.

preferred orientation with a slight development of three maxima, labelled 1, 2 and 3, corresponding to the usage of Schmid *et al.* (1987) (Fig. 6a, ST2:500). This can also be just seen in the ODF section (Fig. 7b). The sample with the next highest strain (sl1:3.5) shows the clear development of two maxima (1 and 3), with the maximum 3 shifted a few degrees clockwise from that of ST2:500. The maximum 2 is present in the extremely tenuous form of a small increase from the background level (Fig. 5c). The weak development of maximum 2 in these experiments compared to those of Schmid *et al.* (1987) is attributed to the influence of the initial preferred orientation, which had the pattern shown in Fig. 6(f). This initial orientation supplied many *c*-axes to the maximum 2 in the Schmid *et al.* (1987) experiments. The initial distribution of *c*-axes for the experiments reported here had only a weak concentration of *c*-axes in orientations that can rotate to maximum 2 (Fig. 5a).

Comparison of the ODF of sl1:3.5 (Fig. 7b) with that of ST2:500 (Fig. 8a) shows that the maxima 1 and 3 are almost identical. Thus, the analysis of Schmid *et al.* (1987) (Fig. 8b–d) of the preferred crystal orientations is also applicable to sl1:3.5. Schmid *et al.* (1987) note that the maxima 2a, 2b and 3 align the *r* plane, the *f* and again the *r* plane, respectively, parallel to the shear plane normal, with the shear direction (s.d.) of those slip systems close to the macroscopic shear direction. Maximum 1 corresponds to the basal plane aligned parallel to the shear plane, but there is little preference of directions in the basal plane to align parallel to the shear direction.

Inverse pole figures

The inverse pole figures (Fig. 9) show a progressive development from being dominated by the initial preferred orientation to the pattern of the high strain single *c*-maximum texture. In the latter, there is a high concentration at *c* with a shoulder to *r* for the shear plane normal and a broad concentration from *m* to *a* for the shear direction. The intermediate strain specimen (sl1:3.5) has an additional maximum of the shear direction close to the shear direction of the *r* and *f* slip systems.

DISCUSSION

In the absence of selective recrystallization or twinning, preferred orientation develops as a result of lattice rotations resulting from dislocation movement. For each element in orientation space, there is a rate of lattice rotation. The evolution of a preferred orientation is the effect of these lattice rotations in modifying the probability distribution. There may be orientations that increase in probability because there tends to be a

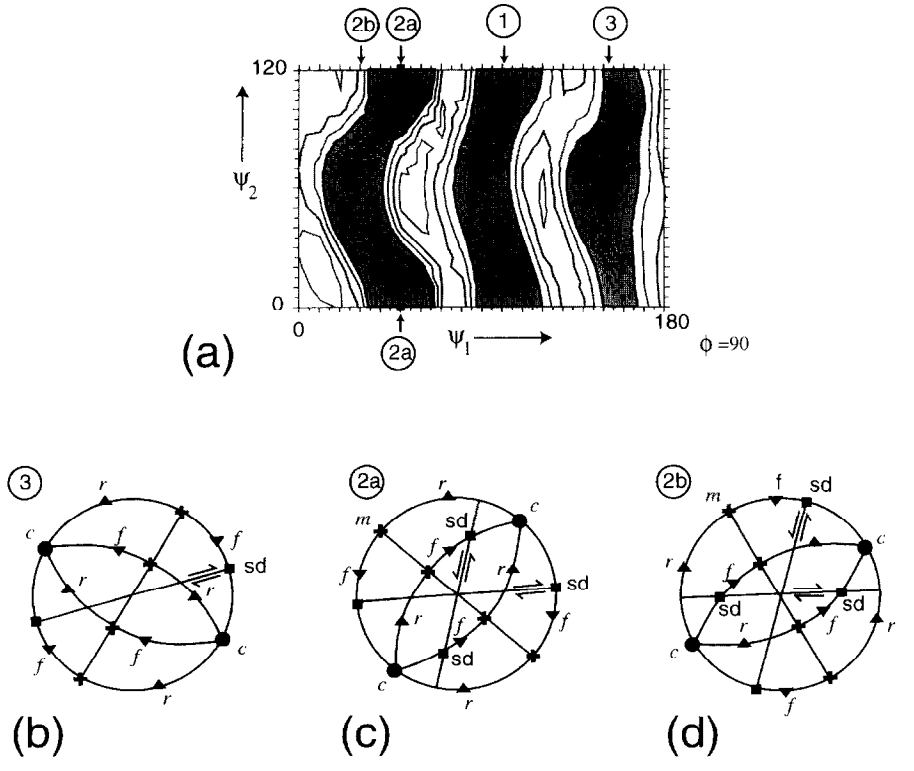

Fig. 8. Analysis of specimen ST2:500 of Schmid *et al.* (1987). (a) Section through the orientation distribution function for $\phi = 90°$. The section is contoured with an interval of 0.25 times uniform. Areas above 1.0 are shaded. (b)–(d) Favoured crystal orientation corresponding to positions 3, 2a and 2b indicated by squares in (a).

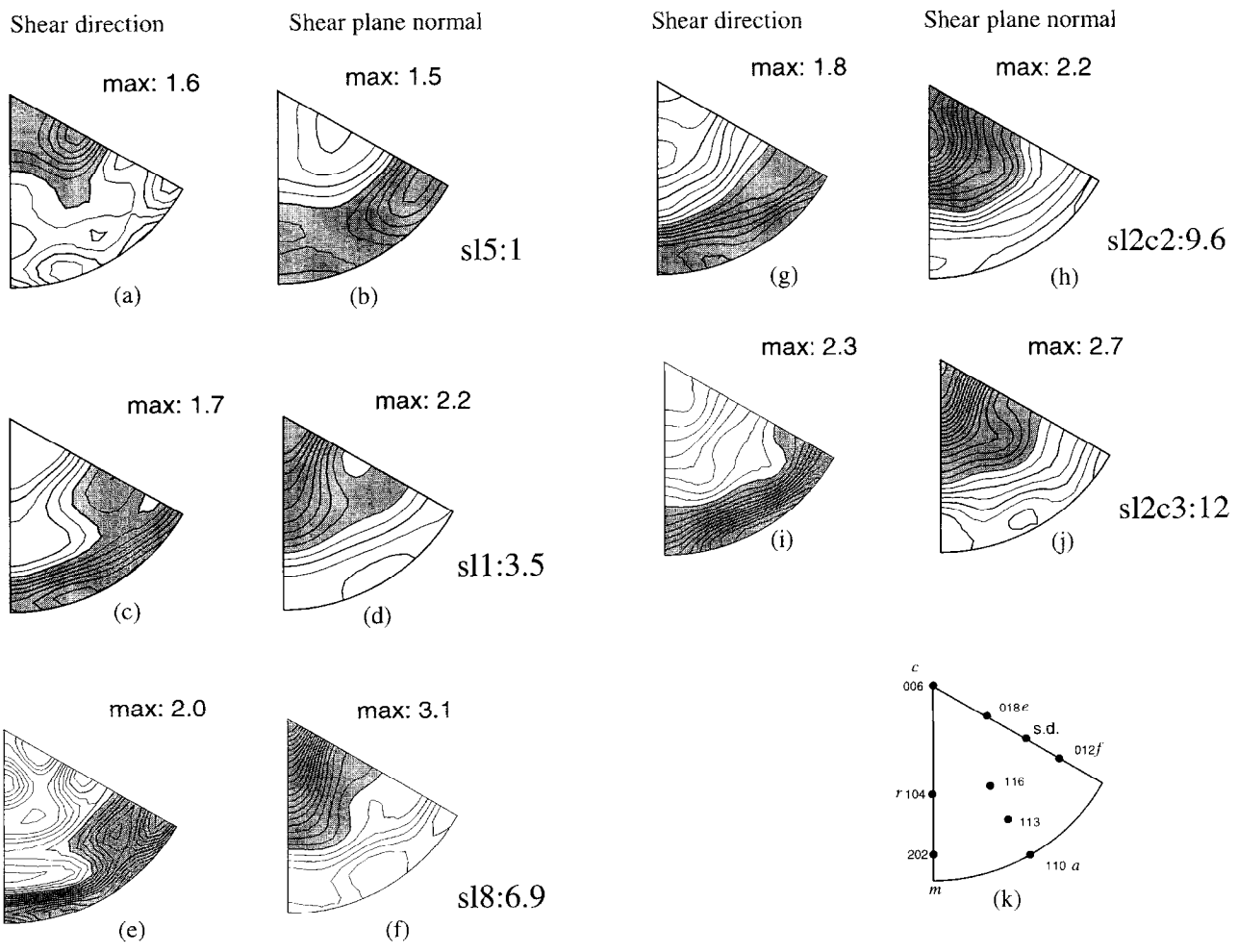

Fig. 9. (a)–(j) Inverse pole figures for the shear direction and the shear plane normal. (k) Orientations of crystallographic directions for calcite. The orientation marked s.d. is the shear direction for the r and f slip systems. The figures are upper-hemisphere equal area projections. The contour interval is 0.1 times uniform. Areas above 1.0 are shaded.

convergence of rotations to these orientations. Conversely, there may be orientations for which the probability decreases because the rotations diverge from these orientations. The lattice rotations throughout orientation space can be regarded as a velocity field, and a useful approach is to apply the conservation law to the probability distribution and the velocity field (Clement and Coulomb, 1979; Clement, 1982). The development of preferred orientation described by the continuity equation is, in words:

$$\text{texture change} = \text{convection} + \text{diffusion} \qquad (1)$$

or mathematically:

$$-\frac{d\rho}{d\gamma} = \mathbf{v}.\text{grad}\rho + \rho\text{div}\mathbf{v}, \qquad (2)$$

where ρ is the probability density or ODF, and $\mathbf{v}$ is the velocity of lattice rotation at a given orientation, expressed in rate of change of orientation with applied shear strain. The first term of the right hand side is a convective term corresponding to the transport of existing maxima and minima of the ODF. The second term is a diffusive term corresponding to concentrations or rarefactions caused by spatial variation of the velocity. The preferred orientation of c-axes for sample sl5:1 (Fig. 5b) is dominated by the convective transport of the initial Solnhofen limestone preferred orientation with some development of maxima due to the diffusion term of equation (1). The results of direct shear experiments in the grain boundary sliding regime, samples ST7:800 and ST4:900 of Schmid *et al.* (1987) (Fig. 6d & e) are almost completely dominated by convective modification. Since the latter experiments were carried out in the grain boundary sliding regime, grain boundary sliding appears to result in the same rigid rotation of all grains, with a rotation rate close to the vorticity of the imposed deformation (0.5 $\dot{\gamma}$).

The sequential development of the preferred orientation with increasing gamma is found to be from (1) two maxima plus a weak third, through (2) two maxima, to (3) a single maximum. This indicates that temporarily, the diffusive development of maxima can dominate over the convective transport, but that the convective trans-

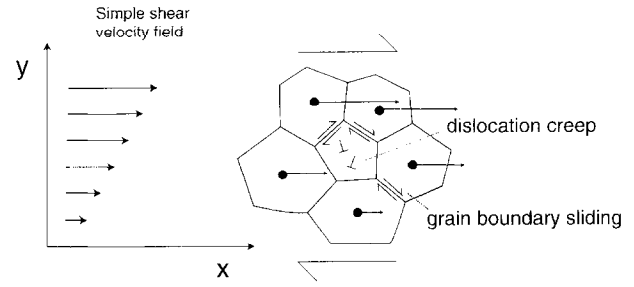

Fig. 10. Simple shear flow field and diagram of some grains deforming by grain boundary sliding and dislocation creep. The velocity field exerts a turning effect on the centre grain.

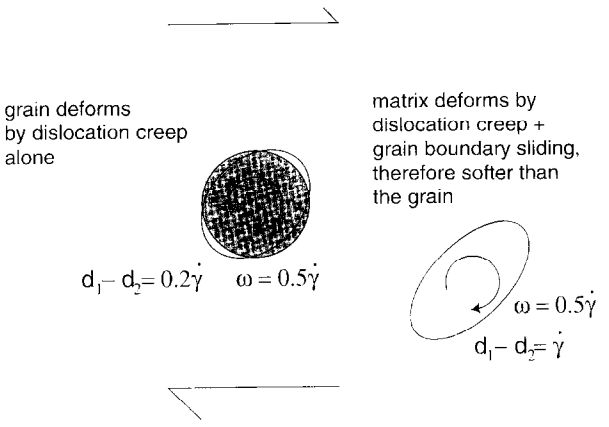

Fig. 11. The deformation of a single grain deforming by dislocation creep surrounded by the aggregate of the rest of the material deforming by dislocation creep and grain boundary sliding. The grain is effectively more viscous than the matrix because it deforms by only one mechanism. The angular rotation rate of both grain and matrix is generally that of simple shear $\omega = 0.5\dot{\gamma}$, whereas the matrix has the differential deformation rate of simple shear $d_1 - d_2 = \dot{\gamma}$, and the grain will have a reduced deformation rate, here arbitrarily set to $d_1 - d_2 = 0.2\dot{\gamma}$. The rotation rate of the grain lattice will be further influenced by angular rotation rates arising from the operation of dislocations.

port wins in the case of maxima 3 and 2 and transports these concentrations to the location of maximum 1.

The high strain results (sl2c2:9.6 and sl2c3:12) indicate that a steady-state texture is being established: that is, the left hand side of equations (1) and (2) are zero, and the convective and diffusive terms balance one another. A consequence of this is that there is no stable end orientation, although the maximum 1 is persistent. Any one grain will rotate continuously with increasing shear strain, spending most time in the vicinity of maximum 1 and rotating rapidly over the intervening orientations.

A possible explanation of the continued rotations is that the deformation is partitioned between grain boundary sliding and intra-crystalline dislocation creep (Fig. 10). The velocity profile across a material deforming by simple shear is shown in the left of the diagram, and a schematic representation of grains deforming by dislocation glide and diffusion accommodated grain boundary sliding is shown on the right. The relative velocity of some of the grain centroids is also shown. It can be seen that the effect of the simple shear velocity field will be to exert a torque on any one grain, for instance, the grain in the centre, which will then tend to rotate bodily.

Figure 11 considers the deformation of any one grain (as a grain and not as a lattice orientation). It will have a rotation rate that is more or less equal to that of simple shear ($0.5\dot{\gamma}$) but a differential deformation-rate ($d_1 - d_2$) that may be significantly less than $\dot{\gamma}$ (the simple shear strain-rate). Thus, it can have a vorticity greater than that of simple shear. Under such conditions, the finite strain of a grain will neither increase continuously nor converge to some limit with increasing shear strain, but will oscillate between zero and some upper bound (Pfiffner and Ramsay, 1982). Thus, the grain shapes will also pulsate within a certain upper bound which is a function of the difference in the grain strain-rate from that of simple shear. Figure 12 is a reproduction of fig. 4 of Pfiffner and Ramsay (1982), with the curves labelled with the factor α, which is the ratio of the actual differential strain rate and that of simple shear. The factor α translates directly to the proportion of the shape change taken up by dislocation creep. It can be seen from the curve for $\alpha = 0.27$ in Fig. 12 that if 27% of the shape

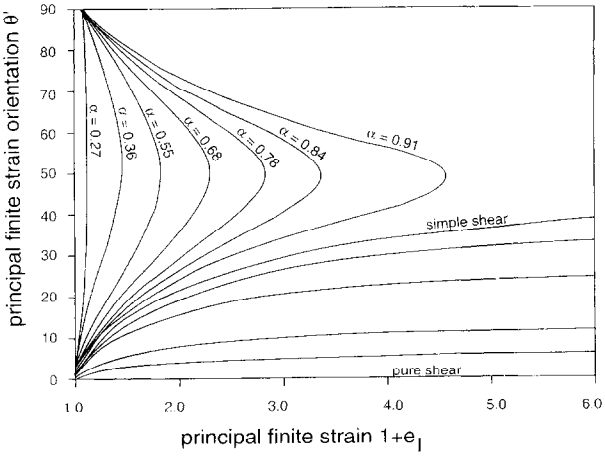

Fig. 12. Orientation of finite strain vs principal finite strain for deformations of varying ratio of strain-rate to angular rotation rate. As the deformation proceeds the strain state moves from the origin along the corresponding curve. For deformations with a ratio of spin to strain-rate greater than that of simple shear the finite strain does not increase to infinity, but reaches a maximum and then falls again (after Pfiffner and Ramsay, 1982).

change occurs by dislocation creep, the maximum grain ratio of long to short axis of the grains is 1.25.

Application to natural mylonites

The preferred orientation observed in natural mylonites is relatively weak in relation to the large finite strains involved. Schmid *et al.* (1981) report *c*-axis concentrations no greater than five times uniform for the lower limb of the Morcles nappe, where the strain is estimated to be $\gamma > 10$ (Ramsay and Huber, 1983). The tendency to a steady-state preferred orientation observed in the experiments could be an explanation for this relatively

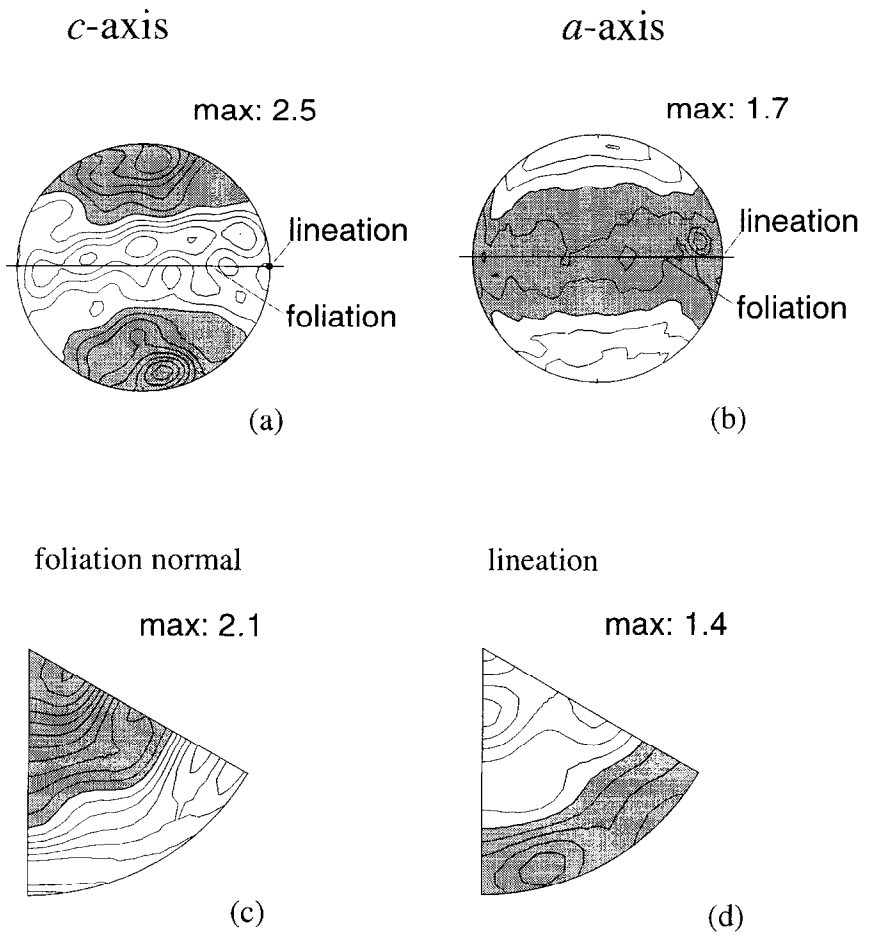

Fig. 13. (a) *c*-axis, and (b) *a*-axis pole figures for an ultramylonite from the Ivrea–Verbano zone of the European Alps. The sense of shear is dextral. Inverse pole figures for the foliation (c) normal and (d) lineation. The figures are upper-hemisphere equal area, with contours of multiples of a uniform distribution. Areas with a value greater than one are shaded grey. The contour interval for the pole figures is 0.2 and for the inverse pole figures is 0.1.

weak preferred orientation. Figure 13 shows the preferred orientation of a calcite ultramylonite from the Ivrea–Verbano zone (Khazanehdari *et al.*, 1998). The *c*-axis pole figure shows a maximum close to the foliation-normal, but slightly displaced towards the shortening direction of the imposed dextral shearing. The *a*-axis pole figure shows a girdle perpendicular to the *c*-axis maximum, and the axis of the girdle is slightly tilted in an anticlockwise direction, again towards the shortening direction of the shearing. Similar *c*- and *a*-axis pole figures are obtained from the majority of calcite mylonites, see Schmid *et al.* (1981). Khazanehdari *et al.* (1998) conclude that the specimen shown in Fig. 13 suffered grain-size reduction by dynamic recrystallization followed by diffusion- plus plasticity-accommodated grain boundary sliding.

The *c*- and *a*-axis pole figures of Fig. 13 show a good first-order agreement with the high strain pole figures of the experiments in Fig. 5(d–f) for the *c*-axis and Fig. 5(j–l) for the *a*-axis. That is, the experimental results show a maximum of *c*-axes close to the shear plane normal but displaced towards the compression direction. The axis of the *a*-axis girdle is displaced in accordance with the displacement of the *c*-axis maximum. However, the girdle in the naturally deformed sample has no sub-maxima, contrasting to the clearly defined sub-maxima of the experimentally deformed sample.

The inverse pole figures for the foliation normal and the lineation also show a good first-order agreement with those for the shear plane normal and shear direction of the high strain experiments, respectively. A closer comparison reveals some differences: the maximum in the inverse pole figure for the foliation normal is displaced towards the *e* pole (see Fig. 9k), whereas for the experimentally deformed material, the maximum is at *c* with a shoulder towards the *r* pole. Specimen 71 of Schmid *et al.* (1981) has an inverse pole figure for the foliation normal that is almost identical with those of the high-strain experiments, but its inverse pole figure for the lineation direction is no longer similar to those of the shear direction in the experiments.

CONCLUSIONS

(1) Large strains are necessary before steady-state

behaviour, in general, and a final preferred orientation, in particular, are attained. The torsion experiment offers a unique opportunity to achieve these kinds of high strains in the laboratory.

(2) Simple shear experiments and torsion experiments approximating simple shear on Solnhofen limestone deforming at the boundary of flow regimes 2 and 3 tend to a steady-state preferred orientation.

(3) Partitioning of deformation on the grain scale into inter-crystalline and intra-crystalline deformation mechanisms can give a sub-equant microstructure without significant recrystallization for high simple-shear strains.

(4) Natural calcite mylonites have preferred orientations that compare very well, but not perfectly, with those of high-strain torsion experiments.

Acknowledgements—Mervyn Paterson and Iona Stretton are thanked for help with the deformation experiments. We are grateful for comments on an early version of the manuscript from Jean-Pierre Burg and Stefan Schmid. Ernie Rutter kindly gave encouragement and suggested Solnhofen limestone as a suitable material for study. Financial support of the Swiss Nationalfonds is gratefully acknowledged. A joint Swiss Nationalfonds British Council exchange grant promoted a fruitful cooperation with the laboratory in Manchester. Graham Price and an anonymous referee are thanked for comments that contributed to an improvement of the manuscript. Sue Treagus as editor made many helpful suggestions for significant improvements in the manuscript for which M. Casey is very grateful.

REFERENCES

Adams, B. L., Wright, S. I. and Kunze, K. (1993) Orientation imaging: The emergence of a new microscopy. *Metallurgical Transactions* **24A**, 819–831.

Bunge, H.-J. (1969) *Mathematische Methoden der Texturanalyse*. Akademie-Verlag, Berlin.

Bunge, H.-J. and Wenk, H. R. (1977) Three dimensional texture analysis of three quartzites (trigonal crystal and triclinic specimen symmetry). *Tectonophysics* **40**, 257–285.

Casey, M. (1981) Numerical analysis of X-ray texture data: an implimentation in FORTRAN allowing triclinic or axial specimen symmetry and most crystal symmetries. *Tectonophysics* **78**, 51–64.

Casey, M., Rutter, E. H., Schmid, S. M., Siddans, A. W. B. and Whalley, J. S. (1978) Texture development in experimentally deformed calcite rocks. In *Proceedings of ICOTOM 5*, Vol. 2, eds G. Gottstein and K. Lucke, March 1978, Aachen, pp. 231–240.

Clement, A. (1982) Prediction of deformation texture using a physical principle of conservation. *Materials Science and Engineering* **55**, 203–210.

Clement, A. and Coulomb, P. (1979) Eulerian simulation of deformation textures. *Scripta Metallurgica* **13**, 899–901.

Dell'Angelo, L. N. and Tullis, J. (1989) Fabric development in experimentally sheared quartzites. *Tectonophysics* **169**, 1–21.

Dietrich, D. and Song, H. (1984) Calcite fabrics in a natural shear environment, the Helvetic nappes of western Switzerland. *Journal of Structural Geology* **6**, 19–32.

Dingley, D.J. and Baba-Kisle, K. (1986) Use of electron back scatter diffraction patterns for determination of crystal symmetry elements. *Scanning Electron Microscopy* **II**, 383–391.

Friedman, M. and Higgs, N. C. (1981) Calcite fabrics in experimental shear zones. *American Geophysical Union Geophysical Monograph* **24**, 11–27.

Handin, J., Griggs, D. V. and O'Brien, J. K. (1960) Torsion of Yule marble under confining pressure. In *Rock Deformation*, eds D. V. Griggs and J. Handin, pp. 245–274. Geological Society of America Memoir **79**.

Kern, H. and Wenk, H. R. (1983) Calcite texture development in experimentally induced ductile shear zones. *Contributions to Mineralogy and Petrology* **83**, 231–236.

Khazanehdari, J., Rutter, E. H., Casey, M. and Burlini, L. (1998) The role of crystallographic fabric in the generation of seismic anisotropy and reflectivity of high strain zones in calcite rocks. *Journal of Structural Geology* **20**, 293–299.

Kunze, K., Adams, B. L., Heidelbach, F. and Wenk, H. R. (1994a) Local microstructural investigations in recrystallized quartzite using orientation imaging microscopy. In *Textures of Materials (Proceedings of ICOTOM 10)*, ed. H. J. Bunge, pp. 1243–1250. Materials Science Forum **157-162**.

Kunze, K., Heidelbach, F., Wenk, H. R. and Adams, B. L. (1994b) Orientation imaging microscopy of calcite rocks. In *Textures of Geological Materials*, eds Bunge, H. J. *et al.*, pp. 127–146. DGM Informationsgesellschaft, Oberursel.

Law, R. D. (1987) Heterogeneous deformation and quartz crystallographic fabric transitions: natural examples from the Moine thrust zone at the Stack of Glencoul, northern Assynt. *Journal of Structural Geology* **9**, 819–833.

Law, R. D., Casey, M. and Knipe, R. J. (1986) Kinematic and tectonic significance of microstructures and crystallographic fabrics within quartz mylonites from the Assynt and Eriboll regions of the Moine Thrust zone NW Scotland. *Transactions of the Royal Society of Edinburgh, Earth Sciences* **77**, 99–126.

Lister, G. S. and Paterson, M. S. (1979) The simulation of fabric development during plastic deformation and its application to quartzite: fabric transitions. *Journal of Structural Geology* **1**, 99–115.

Lister, G. S. and Hobbs, B. E. (1980) The simulation of fabric development during plastic deformation and its application to quartzite: the influence of deformation history. *Journal of Structural Geology* **2**, 355–370.

Lister, G. S., Paterson, M. S. and Hobbs, B. E. (1978) The simulation of fabric development during plastic deformation and its application to quartzite: the model. *Tectonophysics* **45**, 107–158.

Olgaard, D. L. and Evans, B. (1988) Grain growth in synthetic marbles with added mica and water. *Contributions to Mineralogy and Petrology* **100**, 246–260.

Pfiffner, O. A. and Ramsay, J. G. (1982) Constraints on geological strain rates: arguments from finite strain states of naturally deformed rocks. *Journal of Geophysical Research* **87**, 311–321.

Ramsay, J. G. and Huber, M. I. (1983) *The Techniques of Modern Structural Geology, Vol. 1: Strain Analysis*. Academic Press, London.

Riekels, L. M. and Baker, D. W. (1977) The origin of the double maximum of optic axes in quartzite mylonites. *Journal of Geology* **85**, 1–14.

Rutter, E. H. (1974) The influence of temperature, strain rate and interstitial water in the experimental deformation of calcite rocks. *Tectonophysics* **22**, 311–334.

Rutter, E. H. (1984) The kinetics of grain coarsening in calcite rocks. *Progress in Experimental Petrology 6 NERC Series D* **25**, 245–249.

Rutter, E. H., Casey, M. and Burlini, L. (1994) Preferred orientation development during plastic and superplastic flow of calcite rocks. *Journal of Structural Geology* **16**, 1431–1446.

Schmid, S. M. (1976) Rheological evidence for changes in the deformation mechanism of Solnhofen limestone towards low stresses. *Tectonophysics* **31**, T21–T28.

Schmid, S. M., Bolland, J. N. and Paterson, M. S. (1977) Superplastic flow in finegrained limestone. *Tectonophysics* **43**, 257–291.

Schmid, S. M. and Casey, M. (1986) Complete fabric analysis of some commonly observed quartz *c*-axis patterns. In *Mineral and Rock deformation: Laboratory studies—The Paterson Volume*, eds B. E. Hobbs and H. C. Heard, pp. 263–286. American Geophysical Union, Geophysical Monograph **36**.

Schmid, S. M., Casey, M. and Starkey, J. (1981) The microfabric of calcite tectonites from the Helvetic nappes (Swiss Alps). In *Thrust and Nappe Tectonics*, eds K. R. McClay and N. J. Price, pp. 151–158. Geological Society Special Publication **9**.

Schmid, S. M., Panozzo, R. and Bauer, S. (1987) Simple shear experiments on calcite rock: rheology and microfabric. *Journal of Structural Geology* **9**, 747–778.

Venables, J. A. and Harland, C. J. (1973) Electron backscatter patterns – a new technique for obtaining crystallographic information in the SEM. *Philosophical Magazine* **27**, 1193–1200.

Walker, A. N., Rutter, E. H. and Brodie, K. H. (1990) Experimental study of grain-size sensitive flow of synthetic, hot-pressed calcite

rocks. In *Deformation Mechanisms, Rheology and Tectonics*, eds R. J. Knipe and E. H. Rutter, pp. 259–284. Geological Society Special Publication **54**.

Wenk, H.-R., Canova, G., Molinari, A. and Kocks, U.F. (1989) Viscoplastic modeling of texture development in quartzite. *Journal of Geophysical Research* **94B**, 17895–17906.

Wenk, H. R. and Christie, J. M. (1991) Comments on the interpretation of deformation textures in rocks. *Journal of Structural Geology* **13**, 1091–1110.

Wenk, H. R., Venkitasubramanyan, C. S. and Baker, D. W. (1973) Preferred orientation in experimentally deformed limestone. *Contributions to Mineralogy and Petrology* **38**, 81–114.